UC Berkeley
UC Berkeley Previously Published Works

Title

Engineering Relaxor Behavior in (BaTiO3)n/(SrTiO3)n Superlattices

Permalink

Journal

ISSN

Authors

Lupi, Eduardo

Wexler, Robert B

Meyers, Derek

et al.

Publication Date

DOI

Copyright Information

Peer reviewed

Engineering Relaxor Behavior in (BaTiO$_3$)$_n$/(SrTiO$_3$)$_n$ Superlattices

*Eduardo Lupi, Robert B. Wexler, Derek Meyers, Anton Zahradnik, Yizhe Jiang, Sandhya Susarla, Ramamoorthy Ramesh, Lane W. Martin, and Andrew M. Rappe**

Complex-oxide superlattices provide a pathway to numerous emergent phenomena because of the juxtaposition of disparate properties and the strong interfacial interactions in these unit-cell-precise structures. This is particularly true in superlattices of ferroelectric and dielectric materials, wherein new forms of ferroelectricity, exotic dipolar textures, and distinctive domain structures can be produced. Here, relaxor-like behavior, typically associated with the chemical inhomogeneity and complexity of solid solutions, is observed in (BaTiO$_3$)$_n$/(SrTiO$_3$)$_n$ (n = 4–20 unit cells) superlattices. Dielectric studies and subsequent Vogel–Fulcher analysis show significant frequency dispersion of the dielectric maximum across a range of periodicities, with enhanced dielectric constant and more robust relaxor behavior for smaller period *n*. Bond-valence molecular-dynamics simulations predict the relaxor-like behavior observed experimentally, and interpretations of the polar patterns via 2D discrete-wavelet transforms in shorter-period superlattices suggest that the relaxor behavior arises from shape variations of the dipolar configurations, in contrast to frozen antipolar stripe domains in longer-period superlattices (n = 16). Moreover, the size and shape of the dipolar configurations are tuned by superlattice periodicity, thus providing a definitive design strategy to use superlattice layering to create relaxor-like behavior which may expand the ability to control desired properties in these complex systems.

1. Introduction

Superlattices, or unit-cell-precise layered structures, provide researchers with the ability to fine tune competing energy contributions and leverage the interplay of various degrees of freedom in complex oxides to produce emergent phenomena. Those energies and interactions can be further manipulated via epitaxial strain, superlattice periodicity, layer-thickness asymmetry, and other variables, making oxide superlattices a veritable playground for new effects. Superlattices based on alternating layers of ferroelectric and dielectric materials, in particular, have garnered considerable interest due to the prospect of producing exotic polar orders and functionalities, such as improper ferroelectricity, vortex structures, skyrmions, and large piezoelectric responses.[1–3] Such superlattice structures provide researchers with the opportunity to control the energy landscape of materials by manipulating electrostatic, elastic, and gradient energies systematically, thus providing a route to induce exotic order and function. For example, in (PbTiO$_3$)$_n$/(SrTiO$_3$)$_n$ superlattices (where *n* is the number of unit cells), researchers have shown the onset of improper ferroelectricity,[1,4] flux-closure domain structures,[5] and emergent polar structures such as vortices[2,6,7] and skyrmions.[3,8] Superlattice structures have even been used in all-ferroelectric layered structures to enhance ferroelectric polarization and dielectric response simultaneously, as was

E. Lupi, D. Meyers, A. Zahradnik, Y. Jiang, R. Ramesh, L. W. Martin
Department of Materials Science and Engineering
University of California, Berkeley
Berkeley, CA 94720, USA

E. Lupi, S. Susarla, R. Ramesh, L. W. Martin
Materials Sciences Division
Lawrence Berkeley National Laboratory
Berkeley, CA 94720, USA

R. B. Wexler, A. M. Rappe
Department of Chemistry
University of Pennsylvania
Philadelphia, PA 19104-6323, USA
E-mail: rappe@sas.upenn.edu

R. B. Wexler
Department of Chemistry
Washington University in St. Louis
St. Louis, MO 63130, USA

D. Meyers
Department of Physics
Oklahoma State University
Stillwater, OK 74078, USA

ADVANCED
SCIENCE NEWS

www.advancedsciencenews.com

ADVANCED
MATERIALS

www.advmat.de

demonstrated in the $PbZr_{1-x}Ti_xO_3$ system.[9] These examples illustrate the expansive design space and the potential to explore behavior beyond previously reported novel phases and to enhance properties in oxide superlattices.

A superlattice system that has been widely studied is $(BaTiO_3)_n/(SrTiO_3)_n$,[10–12] where $BaTiO_3$ ($SrTiO_3$) is a prototypical ferroelectric (dielectric). As a solid solution, $Ba_{1-x}Sr_xTiO_3$ has also been widely investigated and used for its dielectric properties,[13,14] including nonlinear dynamics[12] and high tunability.[15] As a superlattice, $(BaTiO_3)_n/(SrTiO_3)_n$ has been studied in an attempt to enhance polarization, produce exotic domain structures, etc. In prior work on these superlattices, researchers have reported effects akin to relaxor-like behavior.[16] Despite these intriguing observations, research efforts have been more focused on tuning interlayer strain to produce a broad range of physical properties,[11] and less on explaining the mechanism(s) behind effects such as relaxor-like behavior. The observation of relaxor-like order in superlattice structures with periodic layers is surprising, since relaxor behavior is typically observed in chemically disordered materials.[17–20] For example, in heterovalent relaxors such as $PbMg_{1/3}Nb_{2/3}O_3$ (PMN)[18,21] the B-site cations differ in both valence, size (Mg^{2+} and Nb^{5+} have ionic radii of 72 and 64 pm, respectively), and propensity to displace off center[22] (Mg^{2+} and Nb^{5+} displace by ≈0.08 and ≈0.13 Å, respectively, in lead-based perovskites) giving rise to both electric and elastic random fields that produce relaxor effects.[23] On the other hand, in homovalent relaxors, such as $BaZr_{0.5}Ti_{0.5}O_3$ (BZT), the B-site cations, which are primarily responsible for the onset of polar order, have the same valence but differ in size (Zr^{4+} and Ti^{4+} have ionic radii of 72 and 60.5 pm, respectively, for a 16% size difference) and propensity to displace off center[22] (Zr^{4+} and Ti^{4+} displace ≈0.13 and ≈0.25 Å, respectively) thus resulting in random elastic fields that induce relaxor effects.[24] In these and essentially all relaxors, solid solutions provide local heterogeneous chemical fluctuations that enable disparate competing polar structures with low potential energy barriers between them, leading to a distribution of polar domains, relaxation frequencies, and consequent frequency dispersion of the dielectric response. The $(BaTiO_3)_n/(SrTiO_3)_n$ system, however, lacks most of these relaxor ingredients. There is no random solid solution but orderly layers, and the valences of all A/B cations are +2/+4. Furthermore, the ferroelectric cation (responsible for off-centering) is identically titanium throughout. The A-site Ba^{+2} and Sr^{+2} have ionic radii of 144 and 161 pm, respectively, and this size difference is responsible for $BaTiO_3$ being ferroelectric while $SrTiO_3$ is a dielectric at all temperatures. So many similarities and such a small difference begs the question: can there really be relaxor-like behavior in this chemically and Coulombically ordered superlattice system, and if so, what is the underlying mechanism?

2. Results and Discussion

Here, we explore $(BaTiO_3)_n/(SrTiO_3)_n$ superlattices both experimentally and theoretically, with the goal of investigating the relaxor-like behavior and subsequently explaining the mechanism behind its origin. The current work focuses on symmetric $(BaTiO_3)_n/(SrTiO_3)_n$ ($n = 4, 6, 8, 10, 12, 16,$ and 20 unit cells) superlattice heterostructures with overall film composition of $Ba_{0.5}Sr_{0.5}TiO_3$ epitaxially grown by reflection high-energy electron diffraction (RHEED)-monitored pulsed-laser deposition (Methods). $GdScO_3$ (110) was selected as the substrate due to its lattice parameter ($a_{pc} = 3.96$ Å) being between that of $BaTiO_3$ ($a_{pc} = 4.005$ Å; where pc denotes pseudocubic) and $SrTiO_3$ ($a = 3.905$ Å), and thus it induces moderate in-plane compressive strain on the $BaTiO_3$ (−0.8%) and tensile strain on the $SrTiO_3$ (1.6%). As a comparison, a single-layer $Ba_{0.6}Sr_{0.4}TiO_3$ solid-solution film (henceforth referred to as the single-layer film) was grown for similar measurements. This composition was readily available and is similar in chemical composition and relevant electrical properties, so it serves as a reference ferroelectric material for $BaTiO_3$ layer thicknesses down to ≈3 nm.[25–27] From the behavior of single-layer $BaTiO_3$ films, we expect all $BaTiO_3$ layers in the superlattice structures to be polydomain ferroelectric at room temperature. During the growth of the superlattice heterostructures, persistent and streaky RHEED intensity oscillations indicative of a layer-by-layer growth mode were observed for all depositions, with representative data shown for a $n = 16$ superlattice (**Figure 1**a). $\theta-2\theta$ X-ray diffraction studies reveal single-phase, fully epitaxial, $00l$-oriented films (all 70 nm in total thickness), with superlattice peaks varying as expected according to their superlattice periodicities (Figure 1b). This initial structural characterization shows that high-quality superlattices have been produced. Reciprocal space maps about the 103_{pc}-diffraction conditions of the substrates and superlattices are also consistent with high-quality epitaxial growth (as expected based on the in situ RHEED) and reveal that the heterostructures are all coherently strained to the substrates (Figure S1, Supporting Information). On-axis reciprocal space maps at room temperature about the 002_{pc}-diffraction conditions do not show any peaks at $Q_x \neq 0$ (Figure S2, Supporting Information). This indicates an absence of periodic in-plane features at room temperature (as are observed, for example, in vortex structures in $(PbTiO_3)_n/(SrTiO_3)_n$ superlattices).[2] While $(BaTiO_3)_n/(SrTiO_3)_n$ superlattices are somewhat similar to $(PbTiO_3)_n/(SrTiO_3)_n$ superlattices, there are some differences that may account for the differences in observed polar structures, primarily stemming from the larger and more robust polarization in $PbTiO_3$ compared to $BaTiO_3$ and differences in lattice mismatch to $SrTiO_3$. Z-contrast, high-angle annular dark-field (HAADF) scanning transmission electron microscopy (STEM) imaging further confirms the high quality of the superlattice structures and shows sharp interfaces between the layers, as the Z-contrast primarily comes from barium versus strontium cations (Figure 1c). With this foundation, we proceed to study the evolution of dielectric and ferroelectric properties in these heterostructures.

$SrRuO_3/(SrTiO_3)_n/[(BaTiO_3)_n/(SrTiO_3)_n]_k/SrRuO_3$ capacitor structures (where k is the number of repeat units) were fabricated to enable dielectric and ferroelectric measurements (Experimental Section). Room-temperature polarization-electric field hysteresis loops (**Figure 2**a) reveal no significant remanence but strong polarization values at high fields (17–23 μC cm^{-2}) for all superlattice heterostructures and for the single-layer film. In general, however, the nonlinear response is more pronounced

**ADVANCED
SCIENCE NEWS**

www.advancedsciencenews.com

**ADVANCED
MATERIALS**

www.advmat.de
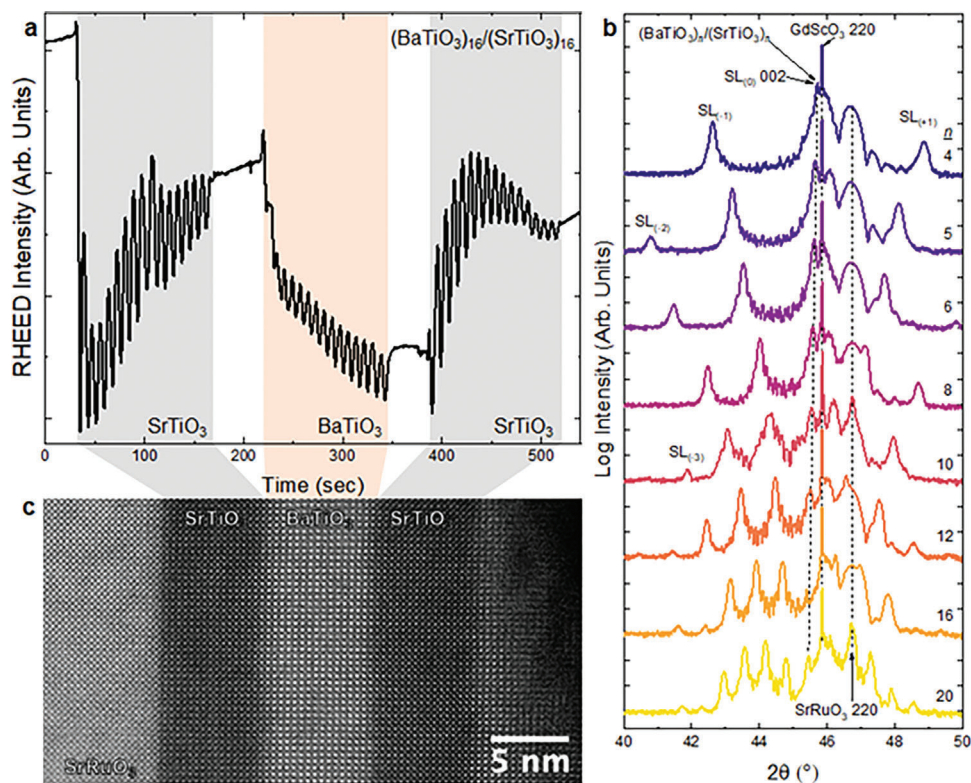
Figure 1. a) Time evolution of the intensity of the 00 specular spot during RHEED-assisted pulsed-laser of a $(BaTiO_3)_{16}/(SrTiO_3)_{16}$ heterostructures demonstrates persistent layer-by-layer deposition control. b) $\theta-2\theta$ X-ray diffraction patterns about the 002-diffraction condition with superlattice fringes varying directly as a function of superlattice periodicity (n). c) HAADF-STEM image confirming sharp interfaces and exacting deposition control in the $(BaTiO_3)_{16}/(SrTiO_3)_{16}$ superlattices.

in short-period superlattices, while long-period superlattices trend more toward linear dielectric response. As compared to the single-layer film (which demonstrates strong nonlinear and nonhysteretic behavior—as expected since the transition temperature ($T_C \approx 250$ K[26]) is below room temperature), the response of the shortest-period superlattices ($n = 4$) is most similar. The lack of remanence in the hysteresis loops at room temperature suggests a lack of stable long-range ferroelectric order in all heterostructures. The single-layer film and all superlattices begin to show some hysteresis upon cooling to 80 K, yet only the single-layer film shows robust remanent polarization consistent with that expected for a ferroelectric below its Curie temperature (Figure S3, Supporting Information).[28] Hysteresis loops for the single-layer film and each superlattice ($n = 4, 6, 8, 10, 12, 16, 20$) at room temperature (Figure S4, Supporting Information) and 80 K (Figure S5, Supporting Information) are provided for clarity. At $n = 4$, the polarization-electric field response is most similar to the single-layer film, suggesting that altering the periodicity down to $n = 4$ can tune the behavior from relaxor-like to a weak conventional ferroelectric.

To investigate the nature of any potential phase transitions in the superlattice heterostructures, temperature- (80–350 K) and frequency-dependent (500 Hz–500 kHz) dielectric measurements were completed on all superlattice variants (Figure 2b). First, the maximum value of dielectric response decreases systematically as the periodicity n increases. Second, the tempera-

ture corresponding to the maximum in the dielectric response (T_{max}) increases as the periodicity n increases. Third, all samples show broad temperature-dependent dielectric peaks and frequency dispersion. To rule out Maxwell–Wagner relaxation as a potential cause of the frequency-dependent enhanced dielectric response,[29,30] dielectric responses (constant and loss) were measured down to a frequency of 100 Hz across the full temperature range (80–350 K) (Figure S6, Supporting Information) and down to 50 Hz at room temperature (Figure S7, Supporting Information). In all cases, no enhancement of the low-frequency (<1 kHz) imaginary response was observed, as evidenced by flat loss tangent and dielectric constant at low frequencies at room temperature and at 150 K (Figure S8, Supporting Information). Despite the absence of Maxwell–Wagner relaxation to account for such effects, prior work has observed similar effects that have been attributed to phenomena as diverse as space-charge relaxation[31] to polaronic relaxation.[32] In this work, broad temperature-dependent dielectric peaks and frequency dispersion are attributed to thermally induced width modulations of domains that enable easily accessible polar fluctuations.

In relaxor ferroelectrics, it is typical to observe a broad temperature-dependent peak and significant frequency dispersion of T_{max} ($\Delta T_{max} = 20$–35 K as the electric-field frequency increases from 500 Hz to 500 kHz for the structures studied here).[33,34] Both of these features are present in all superlattice periodicities studied, but the total dielectric constant and
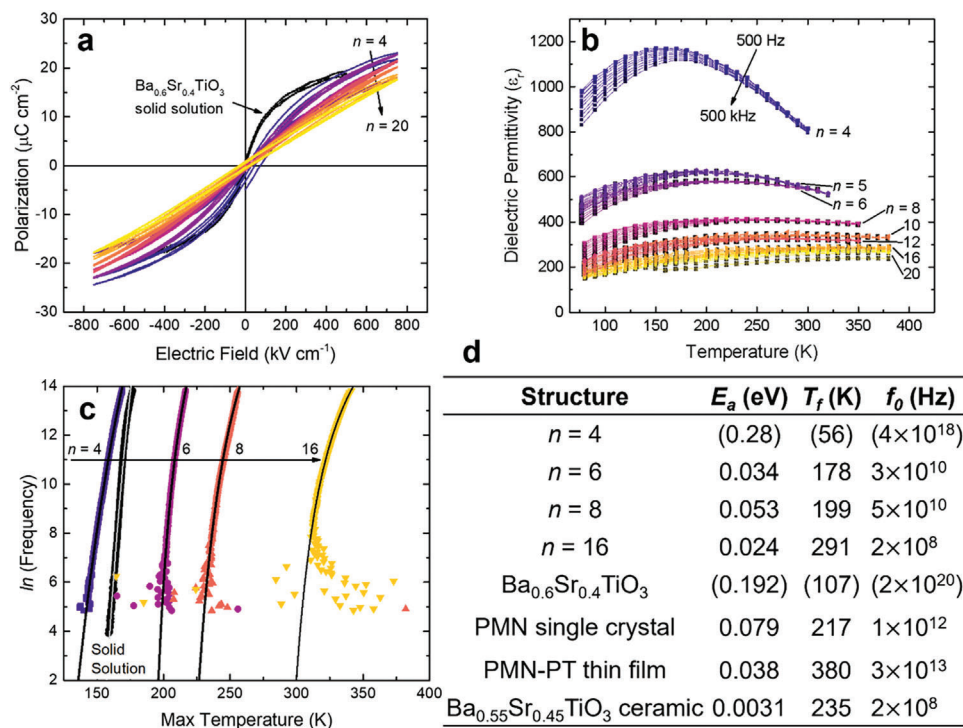
Figure 2. a) Hysteresis loops demonstrate no significant remanent hysteresis across all superlattices and single-layer $Ba_{0.6}Sr_{0.4}TiO_3$. b) Frequency- and temperature-dependent evolution of the dielectric constant for the various superlattices. For each data set, the colors go from bright to dark with increasing frequency (from 0.5 to 500 kHz). c) The frequency- and temperature-dependent data from (b) for selected superlattice periods and the solid-solution film fitted to the Vogel–Fulcher relation. d) Vogel–Fulcher fitted parameters are tabulated.

ΔT_{max} are enhanced in short-period structures. For comparison, the single-layer film has a Curie temperature ≈165 K with essentially no frequency dispersion (Figure S9, Supporting Information). This suggests that, despite having similar chemical compositions, superlattice heterostructures exhibit distinctly different responses from single-layer materials.

The functionality of the short-period superlattices is further illustrated in room-temperature capacitance-voltage measurements which exhibit significant dielectric tunability for the short-period superlattices in response to dc electric fields. The tunability of the dielectric constant when applying a dc field of up to 125 kV cm^{-1} increases from 0% for $n = 16$ superlattices to 24% for $n = 4$ superlattices (Figure S10, Supporting Information). This increase in tunability in the short-period superlattices suggests that either the polarization or the domain structures in these superlattices must be more readily modulated. Likewise, the long-period superlattices have electric-field-independent dielectric constants, which is consistent with the linear shape of their hysteresis loops and is suggestive of larger energy barriers to polarization and/or domain reorientation. Large tunability has been reported in $Ba_{1-x}Sr_xTiO_3$ solid solutions (which has made such materials a focal point for numerous applications),[35,36] and the single-layer films in this study live up to this expectation, with a tunability of 68% at a field strength of 125 kV cm^{-1} (Figure S11, Supporting Information). These observations are consistent with heterogeneous chemical fluctuations in the solid solutions and proximity to the Curie temperature at room temperature. We also note that the static electric-field tunability of the AC di-

electric response of traditional relaxors is larger than that observed in the superlattices here, likely due to the diverse set of local polarization directions in those chemically disordered systems that provide a nearly flat energy landscape. By comparison, the $(BaTiO_3)_n/(SrTiO_3)_n$ superlattices have chemical variation only in a single direction (the out-of-plane direction) and only at ordered interfaces and thus likely possess a lower potential for polarization reorientation than a traditional relaxor. To further explore relaxor-like behavior in this superlattice system, we analyzed the temperature- and frequency-dependent dielectric response using the Vogel–Fulcher relationship (Experimental Section).[37] For brevity and due to the similar nature of the observed responses, we select the $n = 4$, 6, 8, and 16 superlattice heterostructures and the single-layer films for such analyses (Figure 2c). Fitting the data for intermediate- and long-period superlattices to the Vogel–Fulcher equation (Figure 2c, black lines) gives values that agree with existing relaxor literature (Figure 2d).[38] The activation energy E_a ranges between 0.024 and 0.053 eV for all periodicities longer than $n = 4$, and the associated characteristic frequency f_0 values are in the range of 10^8–10^{10} Hz. For traditional relaxors such as single-crystal $PbMg_{1/3}Nb_{2/3}O_3$, thin-film 0.7 $PbMg_{1/3}Nb_{2/3}O_3$-0.3 $PbTiO_3$, and ceramic $Ba_{0.55}Sr_{0.45}TiO_3$, values of E_a and f_0 are in the same range as those noted here for the long-period $(BaTiO_3)_n/(SrTiO_3)_n$ superlattices (Figure 2d).[39] Typical relaxors demonstrate frequency dispersion in their dielectric maxima due to a size distribution of slush-like dynamic polar structures, and they can consequently be fit with the Vogel–Fulcher relationship.[40] On the other hand,

**ADVANCED
SCIENCE NEWS**

www.advancedsciencenews.com

**ADVANCED
MATERIALS**

www.advmat.de
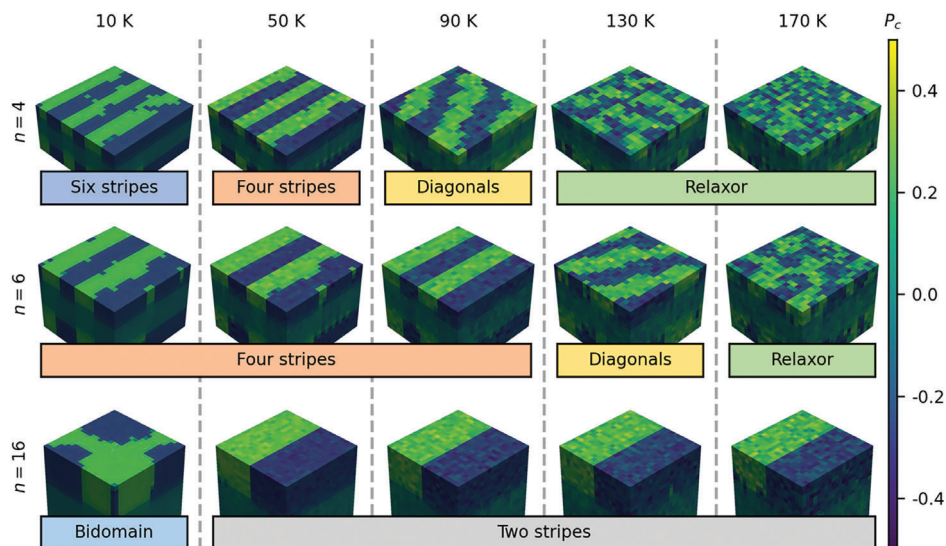
Figure 3. Dipolar configuration-temperature stability diagram for (top) $n = 4$, (middle) $n = 6$, and (bottom) $n = 16$. $n = 4$ has two dipolar configuration transitions ≤ 90 K, whereas the lowest phase transition temperature for $n = 6$ is 130 K. Qualitatively defining T_f as the temperature above which the relaxor-like phase is stable, our results show that $n = 4$ freezes at a lower temperature (90 K) than $n = 6$ (130 K) and $n = 16$ (>170 K), which agrees with the fitted Vogel–Fulcher parameters. The simulation edges are parallel to the [100] and [010] and the vertical direction is the [001]. The color bar has units of C m^{-2}.

robust ferroelectrics such as the Ba$_{0.6}$Sr$_{0.4}$TiO$_3$ single-layer film give an unphysically fast characteristic frequency when fit to the Vogel–Fulcher equation, due to its field-induced transition to a ferroelectric state exhibiting negligible frequency dispersion.[41] For the shortest superlattice period studied in this work ($n = 4$), the unphysically fast characteristic frequency ($\approx 10^{18}$ Hz) is likely explained by a tight distribution of slush-like polar structures, constrained by the electrostatic boundary conditions of the superlattice periodicity. Thus, the fitting of shortest-period superlattices ($n = 4$) to the Vogel–Fulcher relation does not yield a typical relaxor-like characteristic frequency nor activation energy. To denote this, the values obtained for the $n = 4$ and single-layer film are noted in parentheses to indicate the limitations (or failure) of these fits (Figure 2d). This does not mean, however, that the short-period superlattices are simply conventional ferroelectrics, since we still observe frequency dispersion of the dielectric response in addition to an overall enhancement of the response. Furthermore, experimental freezing temperatures (T_f), extracted from the Vogel–Fulcher relationship, increase directly with superlattice periodicity, with T_f rising from 178 K for $n = 6$ superlattices to 291 K for $n = 16$ superlattices. This suggests that smaller, less thermally stable domains are present in the shorter-period superlattices. Taken together, this suggests that the shortest-period superlattices are essentially conflicted—forced into a state that exhibits relaxor-like effects as well as effects more akin to the solid solution. This odd combination, in turn, arises from the superlattice structure placing these materials in intimate contact at the appropriate length scales.

To explain the mechanism behind the experimentally observed relaxor behavior, we analyzed the periodicity- and temperature-dependent evolution of the underlying dipolar structures in the (BaTiO$_3$)$_n$/(SrTiO$_3$)$_n$ superlattices using isobaric–isothermal ensemble (*NPT*) bond-valence molecular dynamics (BVMD) simulations (Experimental Section).

Structural snapshots of the out-of-plane (*c*) component of the polarization (P_c) after finite-temperature equilibration show dipolar configurations with relaxor-like polarization texture for a range of temperatures (horizontal axis, **Figure 3**) and periodicities (vertical axis, Figure 3) in a simulated cell 80 Å in width. At all temperatures, smaller domain sizes are observed in shorter period superlattice simulations, which is consistent with the measured electrical response and nonlinearity. In the short-period $n = 4$ superlattices at temperatures of <50 K, a phase with six antipolar-stripe domains (along the [100] or [010]) per 80 Å forms, as denoted in the *a*–*b* plane of the top interface of each simulation cell. Upon heating to 90 K, the number of antipolar-stripe domains per 80 Å reduces to four, corresponding to an increase in domain width w from 13 to 20 Å. Upon further heating to 110 K, the system favors antipolar-diagonal domains along the [110] or [1$\bar{1}$0], which corresponds with the formation of 28 Å wide stripe domains in the simulation cell. Therefore, at temperatures of ≤ 110 K, the dipolar-structure evolution of the $n = 4$ superlattices upon heating is characterized by a widening of the domains. Above 110 K, a relaxor-like phase composed of slush-like polar structures[23] is observed (i.e., orderings of only a few unit cells), which then disintegrate as other ordering directions and centers emerge. The emergence of a relaxor-like polarization texture above the calculated T_f (90 K for $n = 4$ superlattices) is in excellent qualitative agreement with its strongly temperature- and field-dependent experimental dielectric response. While the thermal evolution of the $n = 6$ superlattice dipolar configuration is similar to that of the $n = 4$ superlattice, the stripe-to-diagonal and diagonal-to-relaxor transition temperatures are higher, and the narrowest ($w \approx 13$ Å) stripe-domain configuration disappears at low temperatures. Finally, for $n = 16$ superlattices, the ground-state dipolar configuration is approximately two antipolar stripe domains per 80 Å for the entire range of simulation temperatures, except for
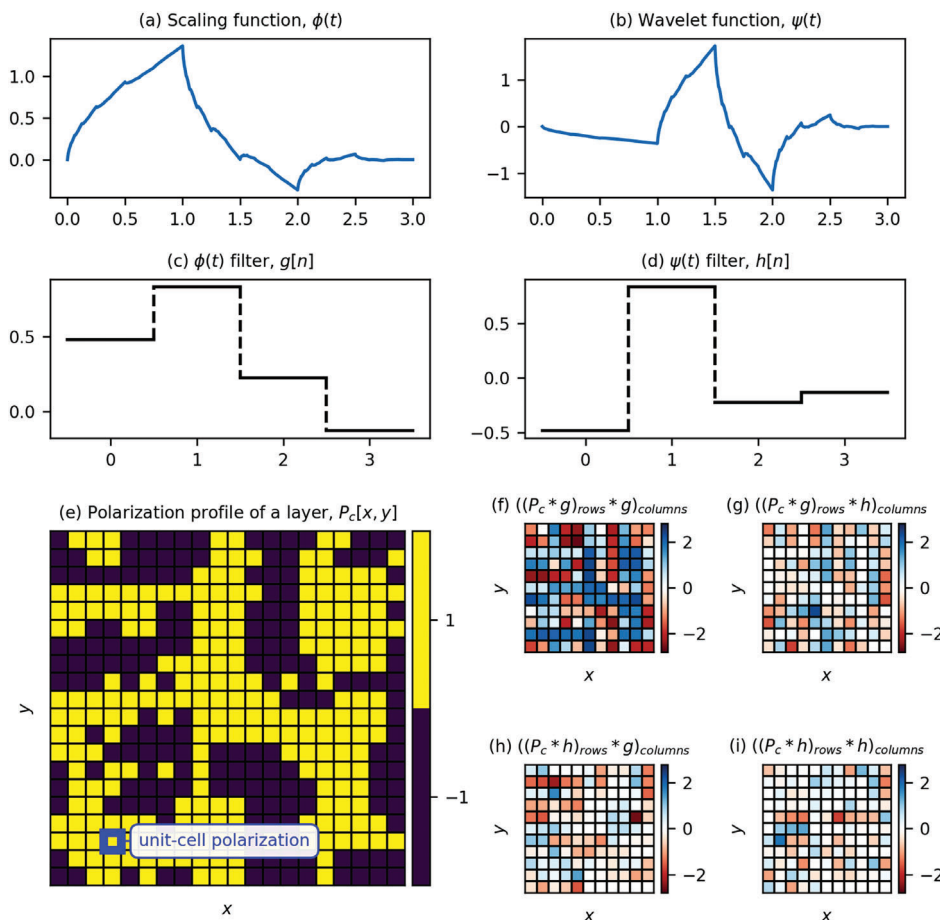
Figure 4. Daubechies db2 wavelets for examining polar order. For image (and polarization-profile) processing, continuous a) scaling and b) wavelet functions are replaced with discrete c) scaling and d) wavelet filters. Starting from e) a 2D polarization profile $P_c = \vec{P} \cdot \hat{z}$, a DWT corresponds to convolutions of P_c and either low-pass g or high-pass h filters. f–i) A one-level 2D-DWT makes four sets of coefficients for the convolution of the rows and columns of P_c and g (so-called "approximation" coefficients) (f), the rows of P_c and g and the columns of that convolution with h (so-called "horizontal detail" coefficients) (g), the rows of P_c and h and the columns of that convolution with g (so-called "vertical detail" coefficients) (h), and the rows and columns of P_c and h (so-called "diagonal detail" coefficients) (i).

simulations at temperatures of <50 K for which there is minor remanence in the time-averaged out-of-plane component of the polarization $\langle P_c \rangle \approx 1.3$ μC cm^{-2}. For this reason, 50 K appears to mark the transition between antipolar-stripe domains ($\geq$ 50K) and robust ferroelectric BaTiO$_3$ layers (<50 K).

To further explore the dynamics of polar domains across the T_f in these systems, we performed 2D discrete-wavelet transforms (2D-DWTs, Experimental Section). The 2D-DWTs used the Daubechies db2 wavelet[42] (**Figure 4**a–d) because 1) they have been used to examine fractal self-similarity,[43–45] which has been observed in relaxor ferroelectrics,[46–48] and 2) the median absolute deviation of their so-called "diagonal detail" coefficients (Figure 4i) estimates the noise level σ_N of a signal or image,[34] which correlates to the polar features of relaxor ferroelectrics because it is proportional to the density and disorder of domain walls (vide infra). It will be shown that for a 2D polarization profile (Figure 4e), instead of an image, σ_N can be used as a polar order parameter ($\sigma_N \to 0$ for a ferroelectric, $\sigma_N > 0$ for a relaxor ferroelectric, and $\sigma_N \gg 0$ for a paraelectric).

Ultimately, we used 2D-DWTs to capture information about spatial order in a 2D image, which, in this case, is the polarization profile (i.e., $P_c = \vec{P} \cdot \hat{z}$, of a [001] layer or the plane normal to the growth direction) in the simulated (BaTiO$_3$)$_n$/(SrTiO$_3$)$_n$ superlattices. Using PyWavelets,[49] we calculated 2D-DWTs by convolving the 2D-polarization profile (i.e., 2D array of P_c values; Figure 4e), and low- and high-pass filters (Figure 4c,d), which are discretized representations of the continuous scaling and wavelet functions (Figure 4a,b). A one-level 2D-DWT produces four coefficient matrices (Figure 4f–i) corresponding to four different convolutions. The matrix elements D_{ij} (same dimensions as original $P_{c,ij}$ image) produced by

$$D = \left(\left(P_c * h \right)_{rows} * h \right)_{columns} \tag{1}$$

are called the "diagonal detail" coefficients (Figure 4i for their matrix and **Figure 5**a for their distribution), where h is the Daubechies db2 wavelet (i.e., high-pass) filter and the subscripts "rows" and "columns" denote the convolution axes. It has been

ADVANCED
SCIENCE NEWS
www.advancedsciencenews.com

ADVANCED
MATERIALS
www.advmat.de
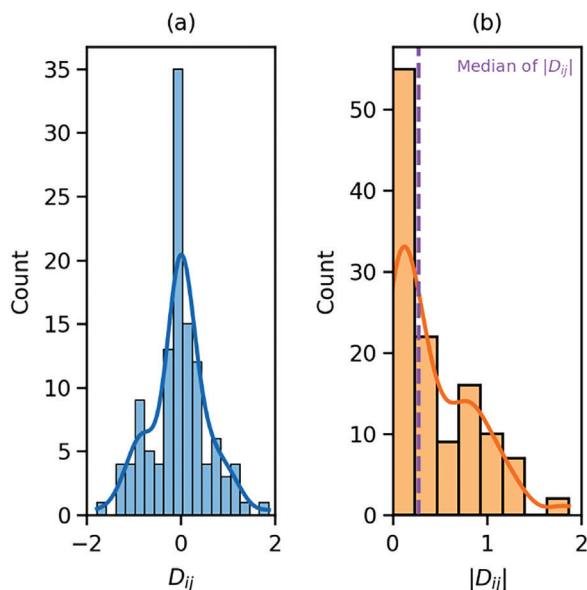
Figure 5. Distribution of: a) the diagonal detail coefficients and b) their absolute values estimating the "polar" noise level (proportional to the median absolute deviation, see purple dashed line and text) from the 2D-DWT of the polarization profile $P_{c,ij}$ in Figure 4e.

proposed that the median absolute deviation of the elements of D, $\{D_{ij}\}$ (Figure 5b), is an accurate estimate of σ_N

$$\sigma_N = \frac{\text{Median}\left(\left|D_{ij}\right|\right)}{PPF(0.75)} \quad (2)$$

where $PPF(0.75) = 0.67$ is the percent point function for the 75th quantile. For a relaxor ferroelectric, we call σ_N the "polar" noise level σ_{PN}.[34]

To understand what σ_{PN} means physically, consider the stripe polarization profile (**Figure 6**a-(i)) and its diagonal detail coefficients (Figure 6a-(ii)). Note, that the difference in the size and number of squares between panels (Figure 6(i),(ii)) results from the down-sampling process inherent to the discrete wavelet transform, where each square in panel (ii) represents the detail information averaged over four neighboring unit cells in panel (i). The coefficients differ from zero only near domain walls. Therefore, Equation (1) acts like an edge detector, finding regions with large polarization gradients. The coefficients are, however, very small (Figure 6a-(iii)), revealing that polarization profiles with well-defined (i.e., less noisy) domains are captured mainly by the Daubechies db2 scaling (i.e., low-pass) filter g and not h. Now consider the random polarization profile (Figure 6b-(i)) and its diagonal detail coefficients (Figure 6b-(ii)). The coefficients are much larger than those of the stripes and normally distributed with a mean of zero; in other words, the random polarization profile is pure polar noise.

To further our understanding of polar noise, we calculate σ_{PN} for a set of systems exhibiting different domain structures. We use the same approach (i.e., perform 2D-DWT, obtain the diagonal detail coefficients, and calculate σ_{PN}) for a ferroelectric, paraelectric, and relaxor ferroelectric; only the values of the coeffi-
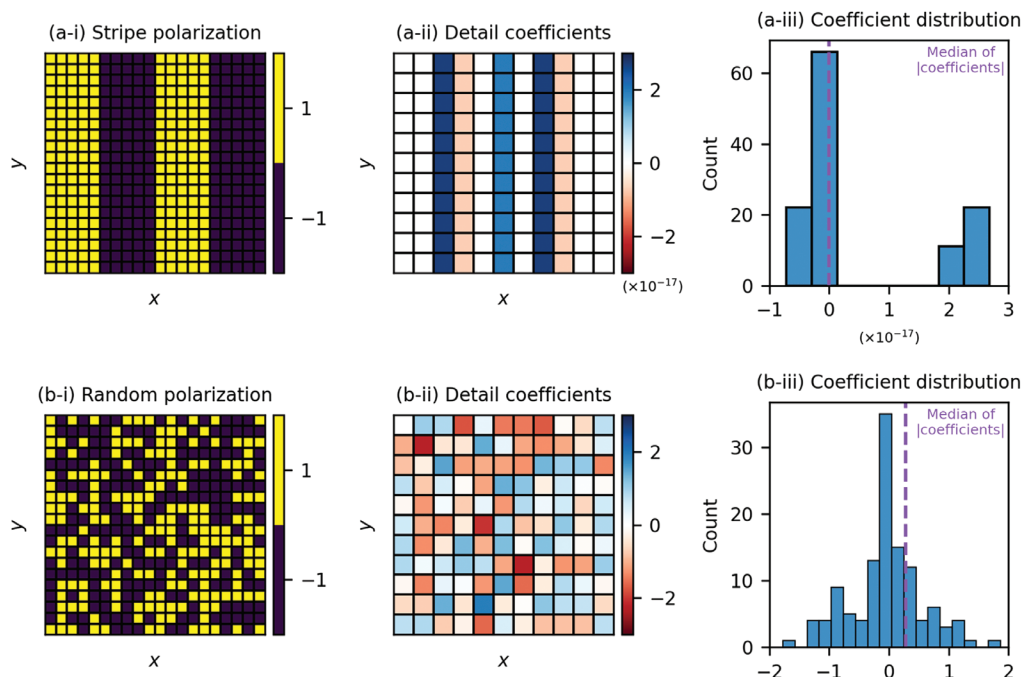
cients and σ_{PN} change when you apply this approach to different 2D polarization profiles. For a monodomain ferroelectric material, long-range order is characterized by large areas of either $+c$ (yellow) or $-c$ (purple) directions (**Figure 7**a-(i)). In this scenario, the diagonal detail coefficients are zero (background turquoise color) and thus $\sigma_{PN} = 0$ (Figure 7a-(ii)); in other words, monodomain ferroelectrics are "noiseless." For a paraelectric material (with random polarization values; Figure 7b), the 2D-DWT yields a larger $\sigma_{PN} = 1.23$ (in units of the wavelet coefficients). Since random polarization values are pure polar noise, we posit that $\sigma_{PN} = 1.23$ is an upper bound for 2D polarization profiles. For a relaxor material at a given time t (Figure 7c) and at some later time (Figure 7d), our polar order parameter is expected to be somewhere between the extreme cases of ferroelectric and paraelectric materials ($0 < \sigma_{PN} < 1.23$) due to the coexistence of ferroelectric- and paraelectric-like phases as slush-like polar structures.[23] Here, for example, the 2D-DWTs for the relaxor yields a $\sigma_{PN} = 0.51$ which could evolve to another intermediate value $\sigma_{PN} = 0.41$.

With this introduction, we apply 2D DWTs to analyze the dependence of polar noise level (vertical axis) on a layer-by-layer basis along the out-of-plane direction (horizontal axis) of the $n = 4$, 6, and 16 superlattices as a function of temperature (color axis) (Figure 7e–g) and use this analysis to quantify the Vogel–Fulcher freezing temperature. For all superlattice periods studied herein, the σ_{PN} in the $BaTiO_3$ layers are less than those for the $SrTiO_3$ at the same temperature. This can be rationalized by the fact that $BaTiO_3$ is not near a phase transition and thus has a well-defined ferroelectric domain configuration, and $SrTiO_3$ is dielectric (an incipient ferroelectric). Additionally, our results show that, across all superlattice periods studied, σ_{PN} decreases with decreasing temperature. This demonstrates that the freezing of polar domains as σ_{PN} decreases corresponds to greater alignment of the dipoles. Since noninterfacial $BaTiO_3$ layers in the superlattices are the closest to bulk $BaTiO_3$ in terms of their local structure and thus ferroelectric behavior, they are likely to serve as the nucleation center from which polar domains can freeze. Therefore, defining T_f as the temperature at which $\sigma_{PN} \to 0$ for noninterfacial $BaTiO_3$ layers, we find that T_f increases with periodicity (from 90 K for $n = 4$, to 130 K for $n = 6$, and finally to >170 K for $n = 16$), which is in excellent agreement with the measured T_f (Figure 2d). Importantly, the 2D-DWTs support the existence of relaxor-like phases in $n = 4$ and 6 superlattices at temperatures greater than T_f, with intermediate dipolar order with values of σ_{PN} between 0.2 and 0.9.

We now rationalize the effect of superlattice periodicity and temperature on the domain width. Again, at a constant temperature, it is observed that the domain width increases with superlattice periodicity. Such a dependence is expected[50,51] for antipolar-stripe domains in ferromagnetic materials and recently generalized for domains in ferroelectric/paraelectric periodic superlattices.[52] Such derivations begin with the following expression for the free energy per unit volume (F) of a ferroelectric thin film of thickness d in an arbitrary dielectric medium

$$F = \frac{\gamma}{w} + F_{elec}(w, d) \quad (3)$$

**ADVANCED
SCIENCE NEWS**
www.advancedsciencenews.com

**ADVANCED
MATERIALS**
www.advmat.de

Figure 6. Two examples, showing: i) the step-by-step procedure for estimating the polar noise distribution for a stripe (a) and random (b) polarization profile. ii,iii) The 2D-DWT produces diagonal detail coefficients (ii) with different distributions (iii).

where γ is the domain-wall energy per unit area and F_{elec} is the electrostatic depolarization energy. Upon applying the latter theory,[52] the relationship between the equilibrium domain width w and superlattice $BaTiO_3$ thickness d is given by

$$w^2 \propto \frac{\gamma \varepsilon_0 \left(\varepsilon_S + \sqrt{\varepsilon_x \varepsilon_z} \right)}{P^2} d \qquad (4)$$

where ε_S is the dielectric constant of the $SrTiO_3$ layers, ε_x (ε_z) is the xx (zz) component of the dielectric tensor for the $BaTiO_3$ layers, and P is the polarization. Qualitatively, this relation suggests that the domain width should increase with increasing periodicity with $w \propto \sqrt{n}$. The intuition behind the positive correlation between domain width and periodicity is that thicker layers (larger d, as in the $n = 16$ superlattices) need larger domain-wall areas for each domain wall. Since the energy cost of creating these domain walls is greater for thicker layers than thinner ones, this favors fewer domain walls per unit length (i.e., wider domains). At a constant superlattice thickness, the domain width decreases with decreasing temperature. This dependence can be understood by considering the measured temperature-dependence of the polarization and dielectric constant in Equation (2). Since the polarization increases ($|P_c|$ increases with decreasing temperature, Figure 3) and the dielectric constant decreases upon cooling below T_f (Figure 2b), the domain width should decrease with decreasing temperature.

Finally, we summarize some directions for future research and discuss some promising strategies for relaxor design via artificial heterostructuring. A natural next step is to explore the effect of asymmetric periodicity on the ferroelectric and dielectric properties of $(BaTiO_3)_n/(SrTiO_3)_m$ superlattices. For example, the stability of polar vortices and vortex mixtures in $(PbTiO_3)_n/(SrTiO_3)_m$ superlattices strongly depends on the period asymmetry $\alpha = n/m$.[53] This raises the following question: is there a critical α for the formation of such exotic polarization states (e.g., relaxors, vortices, skyrmions, etc.) in $(BaTiO_3)_n/(SrTiO_3)_m$ superlattices? A separate avenue for subsequent study is to extend our experiments to other superlattices such as $(Ba_{1-x}Sr_xTiO_3)_n/(SrTiO_3)_m$,[54] $(PbTiO_3)_n/(SrTiO_3)_m$,[53,55–57] $(Pb_{1-x}Sr_xTiO_3)_n/(SrTiO_3)_m$,[55] and $(BaTiO_3)_n/(BaZrO_3)_m$.[58] Such studies, together with examinations of composition-, periodicity-, and composition-plus-periodicity-graded heterostructures, should supply a sufficient set of measurements from which to develop a quantitative theory for relaxor behavior in ferroelectric/paraelectric superlattices.

3. Conclusions

This work studied engineered relaxor behavior in $(BaTiO_3)_n/(SrTiO_3)_n$ superlattices, wherein thermally induced width modulations of antipolar stripe domains are observed in short-period superlattices. Easily accessible polar fluctuations lead to the enhancement of the dielectric constant across a broad temperature range. All experimentally grown superlattices demonstrate some degree of relaxor behavior, with stronger behavior present in shorter periodicities; observations that were predicted and explained by BVMD simulations and wavelet analysis of the resulting polar patterns. We also presented a mechanism for artificially designing relaxor structures in superlattices, wherein the thickness of repeating superlattice units can be modulated to induce relaxor behavior through competition between dipolar configurations (i.e., antipolar-stripe and paraelectric domains) which leads to slush-like polar structures.

ADVANCED
SCIENCE NEWS
www.advancedsciencenews.com

ADVANCED
MATERIALS
www.advmat.de
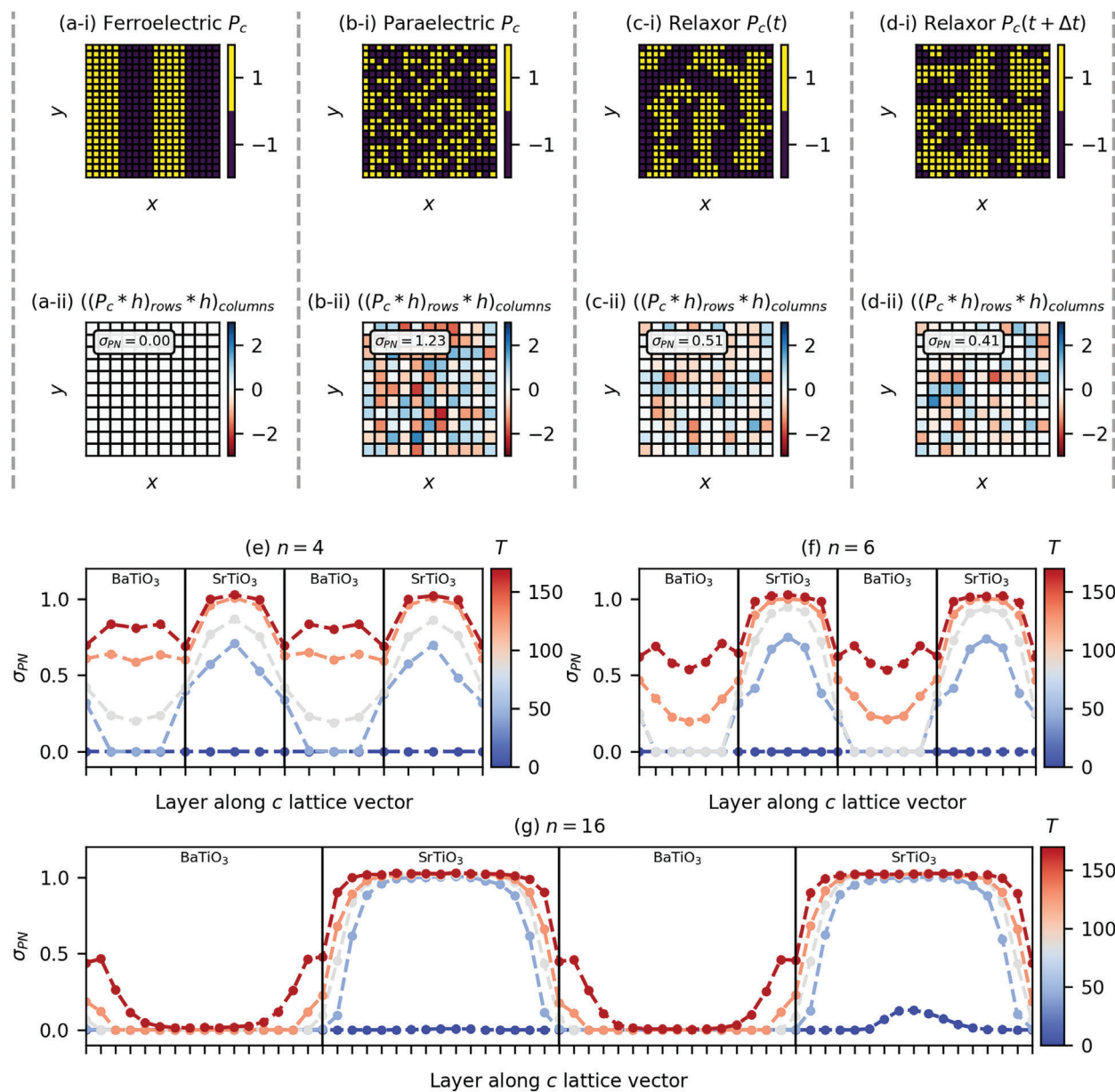
Figure 7. Wavelet-based estimator of the polar noise standard deviation (σ_{PN}). a) 2D discrete wavelet transform of schematic ferroelectric domains (a-i), through a high-pass filter (a-ii) are shown. b–d) Further schematics of a paraelectric (b), relaxor at some time t (c), and the same relaxor at some time later $t + \Delta t$ (d) are shown. e–g) Time-averaged, layer-resolved σ_{PN} for the $n = 4$ (e), $n = 6$ (f), and $n = 16$ (g) superlattices at different temperatures. σ_{PN} and $\Delta\sigma_{PN}$ quantify spatial and temporal order, respectively. σ_{PN} quantifies the spatial dipolar order in each layer along the c-axis. Temporal dipolar fluctuations are given by $\Delta\sigma_{PN}$, i.e., the width of the color bands, where each color band corresponds to a simulation temperature, with dark red at highest simulation temperature (170 K) and dark blue at the lowest simulation temperature (10 K). (e), (f), and (g) support the existence of relaxor-like phases in $n = 4$ and $n = 6$ superlattices at temperatures between 90 and 130 K with intermediate dipolar order with values of σ_{PN} between 0.2 and 0.9 and highly fluctuating dipoles with $\Delta\sigma_{PN} \approx 0.1 - 0.2$.

Finally, this work outlines a pathway for top-down design of relaxational properties in superlattices.

4. Experimental Section

Heterostructure Growth: $(BaTiO_3)_n/(SrTiO_3)_n$ superlattice heterostructures were synthesized via RHEED-assisted pulsed-laser deposi-

tion using a KrF excimer laser (248 nm, LPX-300, Coherent), in an on-axis geometry. 20 nm thick $SrRuO_3$ was deposited (from a ceramic target of the same composition) as a bottom electrode for all heterostructures on GdScO$_3$ (110) single-crystal substrates (Crystec) at a heater temperature of 700 °C in a dynamic oxygen partial pressure of 100 mTorr and a laser fluence of 1.1 J cm^{-2} and laser repetition rate of 10 Hz. BaTiO$_3$ and SrTiO$_3$ were both deposited (from ceramic targets of the same composition) in a dynamic oxygen-partial pressure of 20 mTorr at 700 °C with a laser fluence of 2.1 J cm^{-2} and laser repetition rate of 5 Hz. Superlattices

were always started and finished with a layer of $SrTiO_3$. Top $SrRuO_3$ electrodes were deposited in situ immediately after the $BaTiO_3$ and $SrTiO_3$ superlattice growth, and the entire system was cooled in a static oxygen pressure of ≈ 700 Torr at a rate of 10 °C min^{-1}. All superlattice heterostructures were composed of a 20 nm thick bottom electrode, 70 nm thick superlattice structure, and a 40 nm thick top-electrode layer. A $Ba_{0.6}Sr_{0.4}TiO_3$ solid-solution film was grown for reference in a 40 nm $SrRuO_3$/150 nm $Ba_{0.6}Sr_{0.4}TiO_3$/20 nm $SrRuO_3$ stack on a $GdScO_3$ (110) substrate. This growth was performed at 600 °C in an oxygen partial pressure of 40 mTorr with a laser fluence of 1.52 J cm^{-2} at 2 Hz.

STEM Measurements: Samples for HAADF-STEM were mechanically and subsequently argon-ion milled using Gatan precision ion polishing system (PIPS) starting from 3.5 keV at 4° down to 1 keV at 1° for the final polish. HAADF-STEM experiments were carried out at Lawrence Berkeley National Laboratory using the double aberration-corrected TEAM I microscope operating at 300 kV. The probe semiangle and beam current used for imaging were 30 mrad and 70 pA, respectively.

Fabrication of Capacitor Structures: All measurements were completed on capacitor structures fabricated from the symmetric $SrRuO_3/(SrTiO_3)/(BaTiO_3)_n/(SrTiO_3)_n/SrRuO_3$ heterostructures. To fabricate these structures, large (≈ 200 µm) trenches were ion-milled through the films and into the substrate to provide space to wire-bond. Then, top electrodes were patterned to define 25 µm diameter circular capacitors using photolithography. Next, a 200 nm thick MgO insulating layer was deposited by a room-temperature pulsed-laser deposition process. 80 nm thick platinum pads were sputtered to provide consistent contact between wire-bond and the circular capacitors during temperature-dependent measurements.

Ferroelectric and Dielectric Measurements: Hysteresis loops were measured at a frequency of 10 kHz by a bipolar triangular profile up to 750 kV cm^{-1} using a Precision Multiferroic Tester (Radiant Technologies). Dielectric measurements were carried out using an E4990A Impedance Analyzer (Agilent Technologies) at an ac field excitation voltage of 100 mV and frequency ranges of 50 Hz to 1 MHz using a cryo-cooled probe station (Lakeshore CRX-VF) with wire-bonded contacts to the top and bottom electrodes. Heterostructures were cooled to 77 K and measured upon heating. For Vogel–Fulcher analysis, raw dielectric data was first smoothed to a polynomial to extract the maxima for each temperature sweep at a given frequency. Vogel–Fulcher analysis was performed by fitting the Vogel–Fulcher model

$$f(T_{MAX}) = f_0 \exp[E_a/k_B(T_{MAX} - T_F)] \tag{5}$$

to frequency- and temperature-dependent dielectric maxima using the characteristic frequency f_0, activation energy E_a, and freezing temperature T_F.

Molecular-Dynamics Simulations: To model the dipolar structure and dynamics of the synthesized superlattices, molecular dynamics (MD) simulations in the large-scale atomic/molecular massively parallel simulator (LAMMPS) were performed[59] using the composition-transferable bond-valence interatomic potential for $Ba_{1-x}Sr_xTiO_3$.[28] See ref. [28] for further details about bond-valence-based interatomic potentials, the parameterization of the interatomic potential, and the MD simulations. Every structure is a $20 \times 20 \times 2(n+m)$ supercell containing $4000(n+m)$ atoms and has two periods, i.e., $(BaTiO_3)_n/(SrTiO_3)_m/(BaTiO_3)_n/(SrTiO_3)_m$, in order to include interperiod correlations. To determine the experimentally relevant, minimum-free-energy domain configurations for the $n = 4, 6,$ and 16 superlattices, antipolar stripes, checkerboards, and diagonals of varying width (Figure S12, Supporting Information) were simulated and calculated their time-averaged potential energies vs temperature (Figure S13, Supporting Information). As a point of reference, the Curie temperature of $BaTiO_3$ in BVMD is calculated[60] to be 160 K and experimentally measured to be 393 K.[61] Considering that the experimental measurements are in temperature ranges entirely below 393 K, the simulated temperature range of 10–170 K is appropriate, and the trends from the simulations can be readily mapped to the experimental results. Time averages were taken over the last 0.35 of 1.35 ns *NPT* simulations at equilibrium. Titanium displacements were also initialized of 0.05 Å along [111] so as

to start from the low-temperature ferroelectric and rhombohedral phase of $BaTiO_3$.[62] Dielectric constants and equilibrium polarizations for the equilibrium domain configuration vs temperature were computed. To quantify the spatial and temporal fluctuations of the dipolar structure, the robust wavelet-based estimator of the (Gaussian) noise standard deviation implemented in scikit-image was used.[34,63]

Supporting Information

Supporting Information is available from the Wiley Online Library or from the author.

Conflict of Interest

The authors declare no conflict of interest.

Data Availability Statement

The data that support the findings of this study are available from the corresponding author upon reasonable request.

[1] E. Bousquet, M. Dawber, N. Stucki, C. Lichtensteiger, P. Hermet, S. Gariglio, J.-M. Triscone, P. Ghosez, *Nature* **2008**, *452*, 732.

[2] A. K. Yadav, C. T. Nelson, S. L. Hsu, Z. Hong, J. D. Clarkson, C. M. Schlepütz, A. R. Damodaran, P. Shafer, E. Arenholz, L. R. Dedon, D. Chen, A. Vishwanath, A. M. Minor, L. Q. Chen, J. F. Scott, L. W. Martin, R. Ramesh, *Nature* **2016**, *530*, 198.

[3] S. Das, Y. L. Tang, Z. Hong, M. A. P. Gonçalves, M. R. Mccarter, C. Klewe, K. X. Nguyen, F. Gómez-Ortiz, P. Shafer, E. Arenholz, V. A. Stoica, S.-L. Hsu, B. Wang, C. Ophus, J. F. Liu, C. T. Nelson, S. Saremi, B. Prasad, A. B. Mei, D. G. Schlom, J. Íñiguez, P. García-Fernández, D. A. Muller, L. Q. Chen, J. Junquera, L. W. Martin, R. Ramesh, *Nature* **2019**, *568*, 368.

[4] A. P. Levanyuk, D. G. Sannikov, *Sov. Phys. Uspekhi* **1974**, *17*, 199.

[5] Y. L. Tang, Y. L. Zhu, X. L. Ma, A. Y. Borisevich, A. N. Morozovska, E. A. Eliseev, W. Y. Yang, Y. J. Yang, Y. B. Xu, Z. D. Zhang, S. J. Pennycook, *Science* **2015**, *348*, 547.

[6] A. R. Damodaran, J. D. Clarkson, Z. Hong, H. Liu, A. K. Yadav, C. T. Nelson, S.-L. Hsu, M. R. Mccarter, K.-D. Park, V. Kravtsov, A. Farhan, Y. Dong, Z. Cai, H. Zhou, P. Aguado-Puente, P. García-Fernández, J. Íñiguez, J. Junquera, A. Scholl, M. B. Raschke, L.-Q. Chen, D. D. Fong, R. Ramesh, L. W. Martin, *Nat. Mater.* **2017**, *16*, 1003.

[7] Z. Hong, A. R. Damodaran, F. Xue, S.-L. Hsu, J. Britson, A. K. Yadav, C. T. Nelson, J.-J. Wang, J. F. Scott, L. W. Martin, R. Ramesh, L.-Q. Chen, *Nano Lett.* **2017**, *17*, 2246.

[8] Z. Hong, L.-Q. Chen, *Acta Mater.* **2018**, *152*, 155.

[9] E. Lupi, A. Ghosh, S. Saremi, S.-L. Hsu, S. Pandya, G. Velarde, A. Fernandez, R. Ramesh, L. W. Martin, *Adv. Electron. Mater.* **2020**, *6*, 1901395.

[10] N. Ortega, A. Kumar, O. A. Maslova, Yu. I. Yuzyuk, J. F. Scott, R. S. Katiyar, *Phys. Rev. B* **2011**, *83*, 144108.

[11] N. Ortega, A. Kumar, O. Resto, O. A. Maslova, Yu. I. Yuzyuk, J. F. Scott, R. S. Katiyar, *J. Appl. Phys.* **2013**, *114*, 104102.

[12] S. Hashemizadeh, D. Damjanovic, *Appl. Phys. Lett.* **2017**, *110*, 192905.

[13] C. Ménoret, J. M. Kiat, B. Dkhil, M. Dunlop, H. Dammak, O. Hernandez, *Phys. Rev. B* **2002**, *65*, 224104.

[14] O. G. Vendik, S. P. Zubko, *J. Appl. Phys.* **2000**, *88*, 5343.

[15] S. Y. Wang, B. L. Cheng, C. Wang, W. Peng, S. Y. Dai, Z. H. Chem, *Key Eng. Mater.* **2005**, *280–283*, 81.

[16] H. Tabata, H. Tanaka, T. Kawai, *Appl. Phys. Lett.* **1994**, *65*, 1970.

[17] A. Fernandez, J. Kim, D. Meyers, S. Saremi, L. W. Martin, *Phys. Rev. B* **2020**, *101*, 094102.

[18] F. Li, D. Lin, Z. Chen, Z. Cheng, J. Wang, C. Li, Z. Xu, Q. Huang, X. Liao, L.-Q. Chen, T. R. Shrout, S. Zhang, *Nat. Mater.* **2018**, *17*, 349.

[19] S. Saremi, J. Kim, A. Ghosh, D. Meyers, L. W. Martin, *Phys. Rev. Lett.* **2019**, *123*, 207602.

[20] I. Grinberg, P. Juhás, P. K. Davies, A. M. Rappe, *Phys. Rev. Lett.* **2007**, *99*, 21.

[21] S. Shetty, A. Damodaran, Ke Wang, Y. Yuan, V. Gopalan, L. Martin, S. Trolier-Mckinstry, *Adv. Funct. Mater.* **2019**, *29*, 1804258.

[22] I. Grinberg, M. R. Suchomel, P. K. Davies, A. M. Rappe, *J. Appl. Phys.* **2005**, *98*, 094111.

[23] H. Takenaka, I. Grinberg, S. Liu, A. M. Rappe, *Nature* **2017**, *546*, 391.

[24] C. Laulhé, A. Pasturel, F. Hippert, J. Kreisel, *Phys. Rev. B* **2010**, *82*, 132102.

[25] H. V. Alexandru, C. Berbecaru, A. Ioachim, L. Nedelcu, A. Dutu, *Appl. Surf. Sci.* **2006**, *253*, 354.

[26] R. C. Pullar, Y. Zhang, L. Chen, S. Yang, J. R. G. Evans, P. K. Petrov, A. N. Salak, D. A. Kiselev, A. L. Kholkin, V. M. Ferreira, N. M. Alford, *J. Eur. Ceram. Soc.* **2007**, *27*, 4437.

[27] Y. Jiang, E. Parsonnet, A. Qualls, W. Zhao, S. Susarla, D. Pesquera, A. Dasgupta, M. Acharya, H. Zhang, T. Gosavi, C.-C. Lin, D. E. Nikonov, H. Li, I. A. Young, R. Ramesh, L. W. Martin, *Nat. Mater.* **2022**, *21*, 779.

[28] R. B. Wexler, Y. Qi, A. M. Rappe, *Phys. Rev. B* **2019**, *100*, 174109.

[29] G. Catalan, D. O'neill, R. M. Bowman, J. M. Gregg, *Appl. Phys. Lett.* **2000**, *77*, 3078.

[30] D. O'neill, R. M. Bowman, J. M. Gregg, *Appl. Phys. Lett.* **2000**, *77*, 1520.

[31] O. Bidault, P. Goux, M. Kchikech, M. Belkaoumi, M. Maglione, *Phys. Rev. B* **1994**, *49*, 7868.

[32] O. Bidault, M. Maglione, M. Actis, M. Kchikech, B. Salce, *Phys. Rev. B* **1995**, *52*, 4191.

[33] S. Singh, S. P. Singh, D. Pandey, *J. Appl. Phys.* **2008**, *103*, 2006.

[34] D. L. Donoho, I. M. Johnstone, *Biometrika* **1994**, *81*, 425.

[35] Y. Gim, T. Hudson, Y. Fan, C. Kwon, A. T. Findikoglu, B. J. Gibbons, B. H. Park, Q. X. Jia, *Appl. Phys. Lett.* **2000**, *77*, 1200.

[36] S. G. Lu, X. H. Zhu, C. L. Mak, K. H. Wong, H. L. W. Chan, C. L. Choy, *Appl. Phys. Lett.* **2003**, *82*, 2877.

[37] F. Bahri, H. Khemakhem, M. Gargouri, A. Simon, R. von der Mühll, J. Ravez, *Solid State Sci.* **2003**, *5*, 1445.

[38] D. Viehland, S. J. Jang, L. E. Cross, M. Wuttig, *J. Appl. Phys.* **1990**, *68*, 2916.

[39] S. Ke, H. Huang, H. Fan, *Appl. Phys. Lett.* **2006**, *89*, 87.

[40] Y. N. Huang, X. Li, Y. Ding, Y. N. Wang, H. M. Shen, Z. F. Zhang, C. S. Fang, S. H. Zhuo, P. C. W. Fung, *Phys. Rev. B* **1997**, *55*, 16159.

[41] A. Pramanick, X. P. Wang, C. Hoffmann, S. O. Diallo, M. R. V. Jørgensen, X.-L. Wang, *Phys. Rev. B* **2015**, *92*, 174103.

[42] The Continuous Wavelet Transform, in *Ten Lectures on Wavelets*, Society for Industrial and Applied Mathematics, Philadelphia, PA, USA **1992**, pp. 17–52, https://doi.org/10.1137/1.9781611970104.ch2.

[43] P. Planinšič, A. Petek, *Electrochim. Acta* **2008**, *53*, 5206.

[44] G. Li, K. Zhang, J. Gong, X. Jin, *Proc. CIRP* **2019**, *79*, 500.

[45] A. Scipioni, P. Rischette, G. Bonhomme, P. Devynck, *Phys. Plasmas* **2008**, *15*, 112303.

[46] S. G. Lushnikov, S. N. Gvasaliya, I. G. Siny, *Phys. B: Condens. Matter* **1999**, *263–264*, 286.

[47] J. Hlinka, T. Ostapchuk, D. Noujni, S. Kamba, J. Petzelt, *Phys. Rev. Lett.* **2006**, *96*, 27601.

[48] A. Koreeda, H. Taniguchi, S. Saikan, M. Itoh, *Phys. Rev. Lett.* **2012**, *109*, 197601.

[49] G. Lee, R. Gommers, F. Waselewski, K. Wohlfahrt, A. O'Leary, *J. Open Source Softw.* **2019**, *4*, 1237.

[50] C. Kittel, *Phys. Rev.* **1946**, *70*, 965.

[51] C. Kittel, *Rev. Mod. Phys.* **1949**, *21*, 541.

[52] D. Bennett, M. Muñoz Basagoiti, E. Artacho, *R. Soc. Open Sci.* **2020**, *7*, 201270.

[53] P. Zubko, N. Jecklin, A. Torres-Pardo, P. Aguado-Puente, A. Gloter, C. Lichtensteiger, J. Junquera, O. Stéphan, J.-M. Triscone, *Nano Lett.* **2012**, *12*, 2846.

[54] K. Lim, K. Chew, *AIP Conf. Proc.* **2021**, *2319*, 070001.

[55] P. Zubko, J. C. Wojdeł, M. Hadjimichael, S. Fernandez-Pena, A. Sené, I. Luk'yanchuk, J.-M. Triscone, J. Íñiguez, *Nature* **2016**, *534*, 524.

[56] A. Torres-Pardo, A. Gloter, P. Zubko, N. Jecklin, C. Lichtensteiger, C. Colliex, J.-M. Triscone, O. Stéphan, *Phys. Rev. B* **2011**, *84*, 220102.

[57] P. Zubko, N. Stucki, C. Lichtensteiger, J.-M. Triscone, *Phys. Rev. Lett.* **2010**, *104*, 187601.

[58] A. S. Sidorkin, L. P. Nesterenko, Y. Gagou, P. Saint-Gregoire, E. V. Vorotnikov, A. Yu. Pakhomov, N. G. Popravko, *Sci. Rep.* **2019**, *9*, 18948.

[59] S. Plimpton, *J. Comput. Phys.* **1995**, *117*, 1.

[60] Y. Qi, S. Liu, I. Grinberg, A. M. Rappe, *Phys. Rev. B* **2016**, *94*, 134308.

[61] P. V. Balachandran, D. Xue, T. Lookman, *Phys. Rev. B* **2016**, *93*, 144111.

[62] W. Schildkamp, K. Fischer, Z. Kristallogr, *Cryst. Mater.* **1981**, *155*, 217.

[63] S. Van Der Walt, J. L. Schönberger, J. Nunez-Iglesias, F. Boulogne, J. D. Warner, N. Yager, E. Gouillart, T. Yu, The Scikit-Image Contributors, *PeerJ* **2014**, *2014*, 2:e453.